Enhancement of local electromagnetic fields in plasmonic crystals of coaxial metallic nanostructures

Masanobu Iwanaga*
National Institute for Materials Science, 1-1 Namiki, Tsukuba 305-0044, Japan
and Japan Science and Technology Agency (JST), PRESTO, 4-1-8 Honcho, Kawaguchi 332-0012, Japan

Naoki Ikeda and Yoshimasa Sugimoto
National Institute for Materials Science, 1-2-1 Sengen, Tsukuba 305-0047, Japan
(Received 26 August 2011; revised manuscript received 15 November 2011; published 18 January 2012)

We have experimentally and numerically examined resonant modes in plasmonic crystals (PlCs) of coaxial metallic nanostructures. Resonance enhancements of local electromagnetic (EM) fields were evaluated quantitatively. We clarified that a local mode induced in the coaxial metallic structure shows the most significant field enhancement. The enhancement factors are comprehensively discussed by comparison with other PlCs, indicating that the coaxial PlC provides a locally intense electric field and EM power flux in the annular slit of 50-nm metallic gaps.

DOI: 10.1103/PhysRevB.85.045427 PACS number(s): 73.20.Mf, 78.67.Pt, 81.07.−b

I. INTRODUCTION

Plasmonic crystals (PlCs) of periodic metallic nanostructures have been attracting great interest for more than a decade. Extraordinary transmission (EOT) has led many researchers to investigate the novel optical properties in plasmonic structures; many reports on EOT were reviewed in Ref. 1. In addition to open air-hole structures in single-layer metallic films, coaxial structures also show enhanced transmission and several papers have reported the waveguide modes in coaxial structures, which are associated with the enhanced transmission.[2–10] In these papers, the TEM_0, TE, and/or TM waveguide modes in the annular slits were considered to be the origin of enhanced transmission.

There are other types of resonances in PlCs including coaxial metallic structures. One type is resonances due to periodic structures. Far-field radiation such as plane waves is able to excite surface plasmon polaritons (SPPs) reduced into the first Brillouin zone, and diffraction is simultaneously induced. Another possible type is local resonant modes induced in the metallic nanostructures, which tend to appear as higher modes with flat dispersion and are less often reported because the lower resonances of waveguide modes or reduced SPPs were usually focused in many studies. Local and waveguide modes are discriminated mainly in the field distributions; the latter exhibits Fabry-Perot series in the transmission and reflection spectra as the thickness of waveguide increases.[3] In addition, TE and TM waveguide modes have cutoff frequencies, showing limitation in the excitation wavelength range. Thus waveguide modes, reduced SPPs, and local modes generally coexist in PlCs.

To employ the local plasmonic fields for applications in enhanced spectroscopy such as enhanced absorption[11] and surface-enhanced Raman scattering,[12,13] it is important to select highly field-enhanced resonant modes, whose field enhancements are precisely evaluated. In this paper, we analyze fabricated coaxial PlCs as shown in Fig. 1, examining the resonances and the local electromagnetic (EM) field enhancement.

Experimental and numerical methods are described in Sec. II. Optical properties of PlCs of coaxial metallic nanostructures are measured and analyzed numerically in Sec. III. The enhancement of EM fields at resonances is comprehensively discussed in Sec. IV. The features of coaxial PlCs are summarized in Sec. V.

II. EXPERIMENTAL AND NUMERICAL METHODS

The coaxial PlC shown in Fig. 1 was prepared as follows. An Al film of 150-nm thickness was sputtered on a quartz substrate. A SiO_2 film of 50-nm thickness, which was introduced as a mask for Al film, was sputtered on the Al film. Electron-beam (e-beam) resist was spin-coated and patterned by an e-beam exposure instrument. After development, a mask of the SiO_2 was form by dry etching. Reactive ion etching (RIE) perforates the ring shapes in the Al film. After removing the e-beam resist, plasma-enhanced chemical vapor deposition (PECVD) was conducted to prevent additional oxidation of the Al film and formed SiO_2 of 100-nm thickness in total on the top.

Figure 1(a) shows a top-view scanning-electron-microscope (SEM) image of a fabricated sample. The image presents the coaxial nanostructure of SiO_2. The coaxial structures are hexagonally arrayed with the periodicity of 900 nm. From the SEM image, the outer and inner diameters of the SiO_2 coaxial structures were estimated to be 300 and 200 nm, respectively. The depth profile at the position of the white line is schematically drawn at the bottom of Fig. 1(a); pale blue, dark gray, white denote SiO_2, Al, and air, respectively. Due to the fabrication procedure, the outer and inner diameters of the Al coaxial structures were estimated to be 350 and 150 nm, respectively. As shown later, it turns out that the side walls in the metallic coaxial structures were hardly coated by SiO_2 in the PECVD process.

Transmittance (T) and reflectance (R) spectra were measured in the optical configuration drawn in Fig. 1(b). Incident angle θ was varied in the range of $\theta \geqslant 5^\circ$ in the R measurement. The plane of incidence was set to be parallel to the xz plane. Polarization of the incident plane wave was set to be p ($\mathbf{H}_{in} \parallel y$) or s ($\mathbf{E}_{in} \parallel y$) polarization, where $\mathbf{H}_{in}$ and $\mathbf{E}_{in}$ denote magnetic and electric fields of the incident plane wave, respectively.

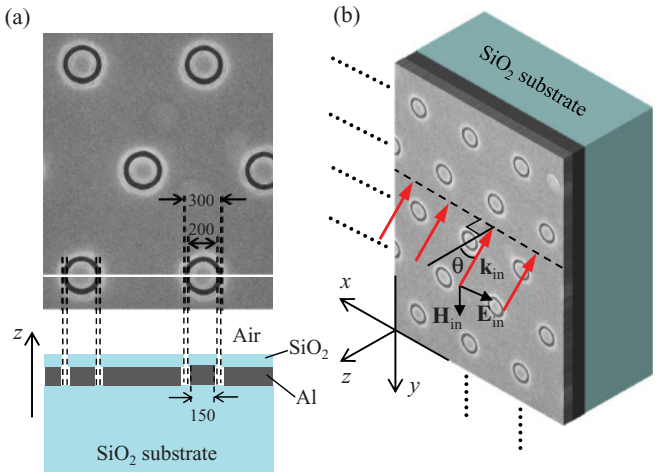

FIG. 1. (Color online) (a) A top-view SEM image of a PlC of hexagonal array of coaxial structures. The periodicity is 900 nm. The depth profile at the white line is drawn at the bottom. The dimensions are in units of nm. (b) Optical configuration: coordinate xyz axes and incident wave vector $\mathbf{k}_{in}$ propagating with incident angle θ. Incident p polarization is drawn as an example.

In the numerical calculations, we employed two methods to investigate linear optical responses. One was the improved Fourier modal method (FMM),[14] which is the most powerful algorithm to compute R and T spectra of layers of periodic structures. By combining the FMM with the scattering matrix method,[15] the R and T spectra of stacked layers composed of periodic structures are stably computed. The R and T were evaluated by using the xy unit cell, which divided by 5×5 nm^2 fine grids. The numerical fluctuations in the computations for the spectra were estimated to be less than 1%. The other method was the finite element method,[16] which is suitable for evaluating EM field distributions in nanostructures because of the flexibility of setting spatial grids to desirable dimensions. Generally, since metallic nanostructures have plasmonic resonances, they need finer spatial grids than dielectric ones. We divided metallic nanostructures with triangles and tetrahedra of sides of less than 5 nm and evaluated EM fields within a-few-percents tolerance. In implementing the two computations, the permittivity of Al was taken from literature,[17] and those of air and SiO_2 were set to be 1.00054 and 2.1316, respectively.

III. RESULTS

Figure 2 shows typical measured and numerically calculated T and R spectra: (a) measured T, (b) calculated T, (c) measured R, and (d) calculated R. The spectra were induced under p polarization. The spectra are shown with offset for clarity: the zero line for each T spectrum is shown with a horizontal bar at the left-hand side, and the 100% line of each R spectrum is shown with a horizontal bar at the right-hand side. In Fig. 2(a), a prominent T peak appears at 1200 nm and $\theta = 0^\circ$, exceeding 20%. At $\theta \neq 0^\circ$, dispersive behaviors are observed; several peaks and dips indicate that plasmonic resonances coexist and interplay in the wavelength range. Figure 2(c) shows that the measured R spectra have dips, complementary to the T peaks.

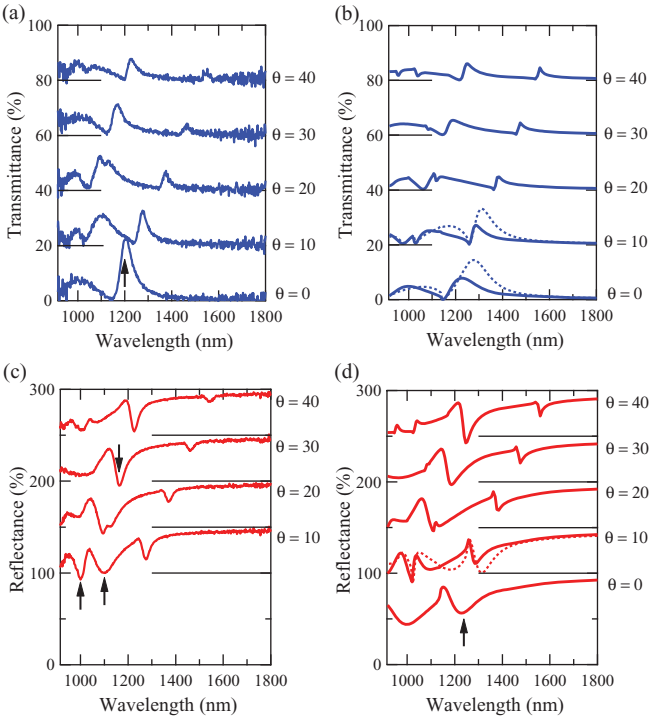

FIG. 2. (Color online) T spectra: (a) measured and (b) calculated. R spectra: (c) measured and (d) calculated. The spectra under p polarization are displayed with offset. The calculated spectra (solid lines) are based on the structure drawn in Fig. 1(a). Dotted lines in (b) and (d) denote the calculated spectra based on the structure first inferred from the fabrication procedure; however, they do not reproduce well the measured data. Arrows indicate the resonances picked up in Table I.

Taking account of the PECVD process, it may be first inferred that all the surfaces are covered by SiO_2. The dotted lines at $\theta = 0^\circ$ and 10° in Figs. 2(b) and at $\theta = 10^\circ$ in 2(d) were evaluated based on the conjecture that the side walls of the metallic nanostructures are covered by SiO_2 up to the area surrounded by the nearest-neighbor dashed lines drawn in Fig. 1(a). From comparison with measured T and R, the resonant wavelengths are inconsistent and the spectral shapes are qualitatively different from the measured spectra, so we do not adopt this depth profile.

To reproduce the experimental data, many depth profiles were tested. The most reproduced profile is shown at the bottom of Fig. 1(a). It was finally found that the side walls of SiO_2 are hardly formed by the PECVD process. Simply neglecting the SiO_2 side walls for Al as shown in Fig. 1(a), the T peaks, R dips, and the spectral shapes were qualitatively reproduced quite well as shown in Figs. 2(b) and 2(d). The measured spectra under s polarization were similarly reproduced by the depth profile. Other structural parameters were taken from the SEM images and the estimated values in the fabrication procedures.

Although the structural model drawn in Fig. 1(a) qualitatively reproduces experimental T and R, some quantitative discrepancies still remain. These are presumably due to the following reasons: (i) not all of the structural parameters are known; for example, the diameters of Al coaxial structures are estimated and not exact, and (ii) the permittivity of Al is

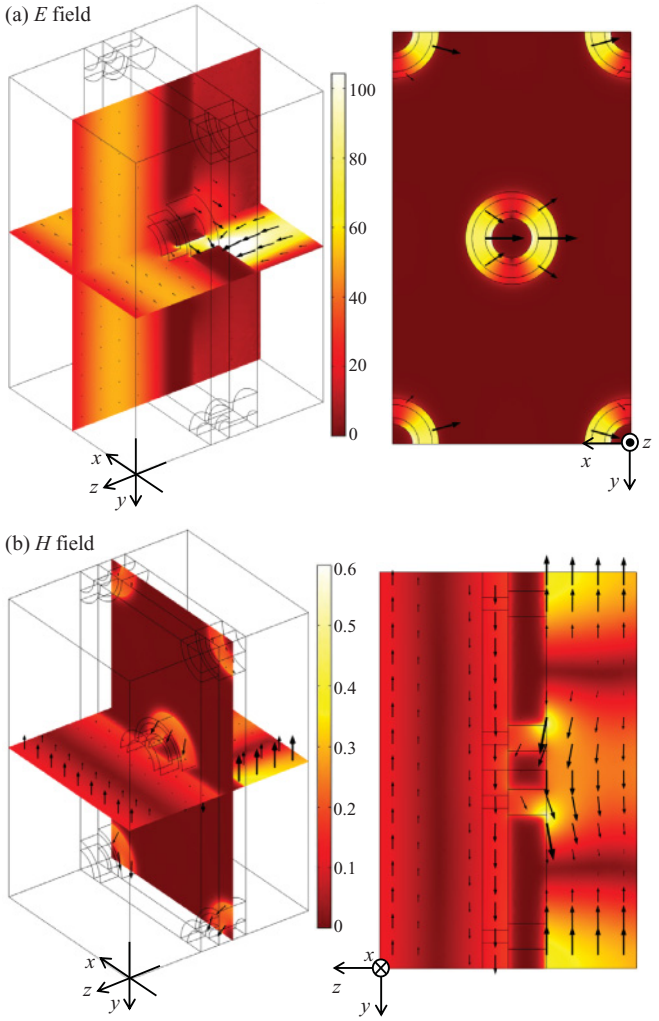

FIG. 3. (Color online) (a) E and (b) H field distributions at a T peak. The incident wavelength is 1200 nm with $\theta = 0°$. The xy section in (a, right) was taken at the center of the layer of Al and air. The yz section in (b, right) was located at the center of the unit domain. The incident electric field $\mathbf{E}_{in}$ is parallel to the x axis. The incident E- and H-field intensities were 27.5 V/m and 7.30×10^{-2} A/m, respectively. The indicators in (a) and (b) are shown in units of V/m and A/m, respectively.

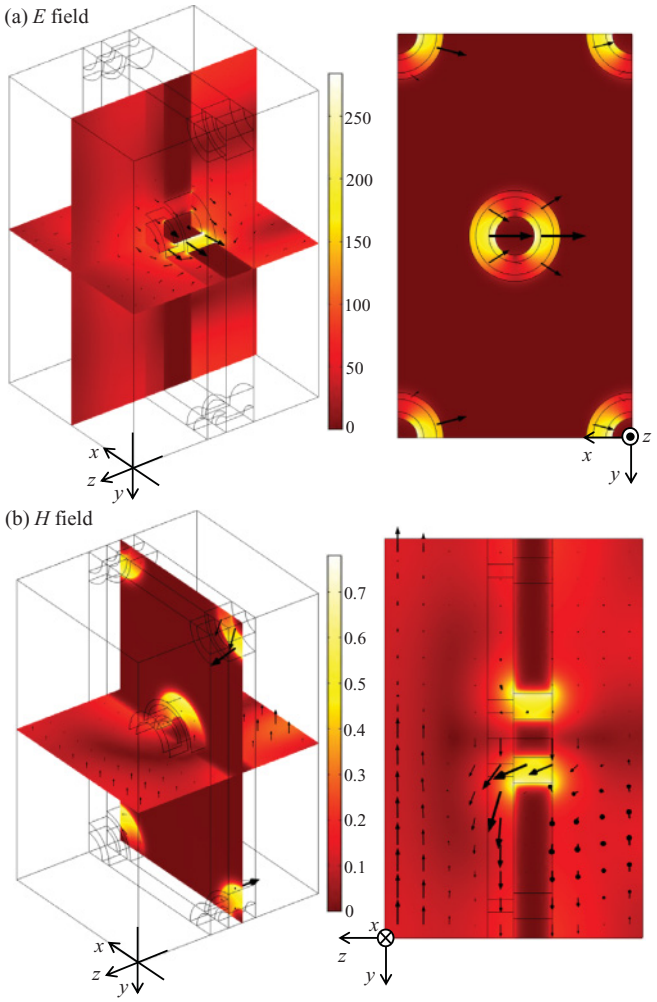

FIG. 4. (Color online) (a) E and (b) H field distributions at a R dip: incident wavelength is 1100 nm and $\theta = 10°$. The incident plane wave is p polarized. The sections and indicators are shown similarly to Fig. 3. The input power are also set similarly.

not the same as that in the literature.[17] However, the qualitative features are reproduced by the depth profile model in Fig. 1(a); it is therefore appropriate to conduct analysis based on the depth profile.

Figure 3 shows EM field distributions under the condition that a T peak appears at 1200 nm and $\theta = 0°$: (a) electric (E) and (b) magnetic (H) fields. As is shown in Fig. 3, a unit domain was set to implement the finite element method.[16] An incident plane wave comes from the xy input port at the left-hand side. Periodic boundary conditions were assigned to the xz and yz boundaries. The field distributions are extracted from representative sections. The xz sections are located at the center of the unit domain. The xy section in Fig. 3(a) (right) was taken at the center of the layer of Al and air. The yz section in Fig. 3(b) (right) was taken at the center of the unit domain. The color plots denote the absolute values of the fields and arrows stand for the three-dimensional (3D) vector fields. The units of indicators are V/m and A/m in Figs. 3(a) and 3(b), respectively, and the intensities are determined by setting the input power to 1.0 W/m^2; accordingly, the E-field intensity was 27.5 V/m and the H-field intensity was 7.30×10^{-2} A/m. Since we focus here on linear phenomena, the intensities are proportional to the input power. The phase of the incident plane wave was defined as $\mathbf{E}_{in} = (1,0,0)$ at the xy input port.

The excited state shown in Fig. 3 is a reduced SPP at the interface between Al PlC and the substrate. The feature is clearly seen in H field distribution. The most enhanced H field appears at the interface with the substrate. The E field is also enhanced in the substrate. In addition, Fig. 3(a) presents that enhanced E field appears in the coaxial structure, as discussed in Sec. IV.

Figure 4 shows EM field distributions under the condition of a broad R dip induced under p polarization at 1100 nm and $\theta = 10°$. The method of presenting the EM field distributions is similar to that in Fig. 3. The excited EM fields are highly enhanced in the coaxial structure, and do not form enhanced fields in air or substrate. Thus the mode is distinct from the reduced SPP mode in Fig. 3 and is ascribed to a local

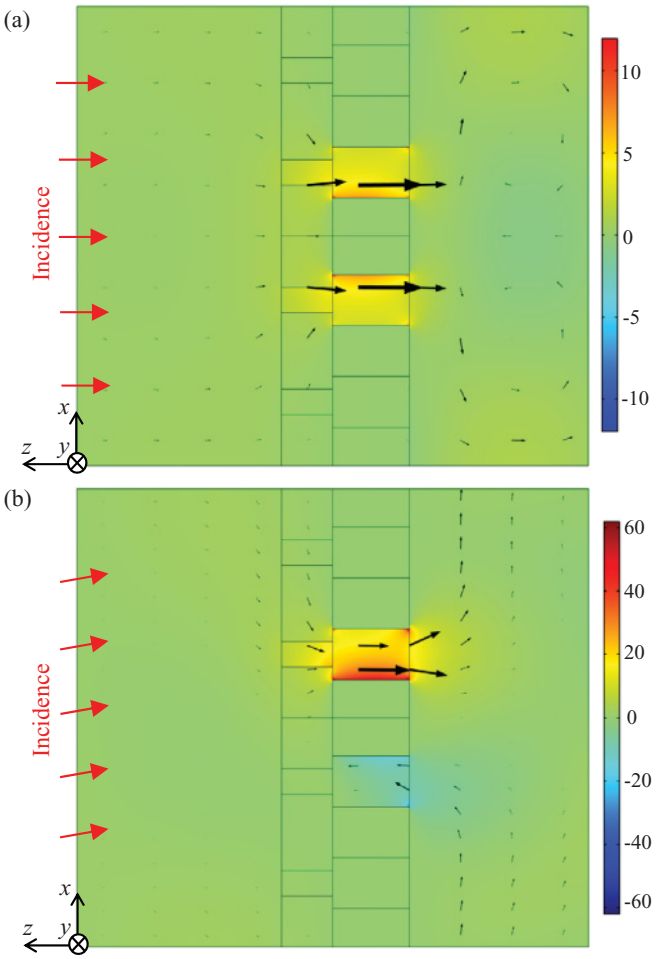

FIG. 5. (Color online) Time-averaged EM power flows: (a) and (b) correspond to the conditions in Figs. 3 and 4, respectively. The xz sections were taken at the center of the unit domain. The indicators are shown in units of W/m^2. Incident wave vectors are drawn at the left edge.

mode induced in the coaxial metallic nanostructure. Let us first clarify that the mode is not a waveguide mode. If the mode is a waveguide mode, a TEM$_0$ or TM mode is possible since the incident plane wave is p polarized and induces TM modes in the PlC. However, TM mode has cutoff wavelength and is expected to be located at far shorter wavelengths;[3] moreover, the power flow in the coaxial structure shown in Fig. 5(b) denies that the mode is a TEM$_0$ mode. In general, waveguide modes hold the power flow independent of the incident angles. In Fig. 5(b), the incident angle is only 10°; nevertheless, a counterflow along the $+z$ direction is evident at the lower slit. Thus the mode at 1100 nm and 10° is not a waveguide mode. We next examine the dispersion. As shown in Fig. 2, the mode is located close to the other modes (or reduced SPPs) at $\theta = 10°$ and overlapped in part at 20°. It is consequently hard to explicitly separate this mode from the other modes; however, this mode is observed at almost the same wavelengths for $\theta = 10°$ and 20° in Fig. 2, suggesting that it is a local mode. By crossing with reduced SPPs, the mode is not observed at $\theta \geqslant 30°$; such disappearance often takes place at the wavelength range where resonances overlap. In contrast, the reduced SPP in Fig. 3 is induced at a wide range of incident angles as seen in Fig. 2. This suggests that the reduced SPP has the largest oscillator strength among the competing resonances.

Figures 5(a) and 5(b) show time-averaged EM power flows, equivalent to Poynting fluxes, under the conditions corresponding to Figs. 3 and 4, respectively. The xz sections were taken at the center of the unit domain. An incident plane wave travels along the $-z$ direction (from left to right) as incident wave vectors are schematically drawn at the left edge. The color plot in units of W/m^2 denotes EM power flow for the z axis and is defined such that the $-z$ direction is positive. Arrows are 3D vectors of the EM power flow on the sections. The EM power flow in Fig. 5(a) is induced at the normal incidence and therefore exhibits a symmetric flow in the coaxial structure. The most intense flow is observed at the ring-shaped slit in the metallic layer. The rotatory flow in the substrate means that the diffraction channel into the substrate is open. On the other hand, the EM power flow in Fig. 5(b) is asymmetric, indicating that a waveguide mode in the annular slit is not induced. The dominant flow is along the $-z$ direction at the ring-shaped slit in the metallic layer. The EM power flow in the substrate is affected by diffraction. In both cases, the EM power flows are dominantly enhanced inside the coaxial metallic structure, and this feature is observed regardless of the type of the resonant mode. At some of other resonances seen in Fig. 2, similar enhancement of EM power flows was observed. The enhancement factors are discussed in the next section.

IV. DISCUSSION

Local E fields in plasmonic structures are often employed to conduct enhanced spectroscopy. Here, we discuss local fields including H and power-flow (P) fields to clarify the potentials to study subwavelength interplay of EM waves with matter. We mention that there are very few reports that comprehensively discuss E, H, and P fields in PlCs.

Table I lists the enhancement factors of E, H, and P fields. The factors are defined as the ratio to the incident fields. The input EM power was 1.0 W/m^2, and the corresponding E- and H-field intensities were already noted in Fig. 3. The maximum intensity of E field on resonances was extracted on the xy section at the center of the Al-air layer as shown in Figs. 3(a) and 4(a). The E-field intensity usually takes the largest absolute value at the sharp edge of a metal; however, such nanostructures are not experimentally feasible and therefore we do not pursue the E field at the edge. Instead, we concentrate on the nanostructures that are well defined and experimentally useful, so that we list the representative maximum values in the PlC without evaluating the slight local modification in structure that is unexpectedly made in the fabrication procedure. The maximum intensity of H field was taken from the yz section across the PlC as shown in Figs. 3(b) and 4(b). As noted in Sec. III, characteristic H field distributions appear on the yz section. The maximum values of P field were taken inside the coaxial structure. The present interest is resonant effects in coaxial PlC; therefore, the effects outside the coaxial structure is out of scope. In fact, significant effects outside the coaxial structure were not observed.

Let us briefly describe the details of the resonant modes listed in Table I. As noted in Sec. III, the resonance at 1200 nm

TABLE I. The top line lists the set of wavelength (nm), incident angle θ, and the polarization that is stated when $\theta \neq 0^\circ$. The corresponding T and R are indicated by arrows in Fig. 2, except for the s-polarized case. The ways to select the maximum intensities of E, H, and P fields are described in the text.

	1200, 0°	1238, 0°	1100, 10°, p	1000, 10°, p	1162, 30°, p	1174, 30°, s
$\lvert\mathbf{E}_{\max}\rvert/\lvert\mathbf{E}_{\text{in}}\rvert$	3.5	6.5	10	4.7	1.5	1.8
$\lvert\mathbf{H}_{\max}\rvert/\lvert\mathbf{H}_{\text{in}}\rvert$	8.1	8.6	8.4	6.6	4.0	4.3
$P_{\max}/P_{\text{in}}$	1.1	15	62	11	2.9	0.6

and $\theta = 0^\circ$ is a reduced SPP at the interface of the Al-PlC and substrate, and that at 1100 nm and $\theta = 10^\circ$ is a local mode excited around the metallic coaxial structure. In Fig. 2(d), a broad R dip indicated by an arrow appears at 1238 nm and $\theta = 0^\circ$. The mode is excited at a lower energy than the reduced SPP at 1200 nm and is different from the reduced SPP. Actually, the EM field distributions are similar to the local mode and show enhanced E, H, and P fields. The P field is locally enhanced inside the annular structure. The mode at 1000 nm and $\theta = 10^\circ$, indicated in Fig. 2(c), is a reduced SPP mode at the interface of the PlC and air and has several-fold enhanced EM fields. In the fabricated sample, the layer of coaxial SiO_2 is inserted between the PlC and air and has the most enhanced H field on the yz section. The mode at 1162 nm and $\theta = 30^\circ$ corresponds to a large R dip as shown in Fig. 2(c) and does not have significantly enhanced EM fields inside the metallic coaxial structure; instead, diffractive field patterns appear in air, suggesting that the mode is associated with diffraction into air. The maximum H-field intensity is located at the positive z side of the Al surface. The mode at 1174 nm and $\theta = 30^\circ$ under s polarization has EM field distributions similar to those of the mode at 1162 nm and $\theta = 30^\circ$. The enhancement factors are also similar. Overall, the most enhanced EM fields were found in the local mode inside the coaxial structure, reaching enhancement factors of more than 10.

As for the field enhancement, we numerically compared the coaxial PlC to an open air-hole PlC that has the same periodicity and air holes of 350-nm diameter, obtained by removing the SiO_2 layer and inner metallic rods of 150 nm in Fig. 1(a). The air-hole PlC has a T peak at 1200 nm and $\theta = 0^\circ$, and the enhancement factors are $|\mathbf{E}_{\max}|/|\mathbf{E}_{\text{in}}| = 1$, $|\mathbf{H}_{\max}|/|\mathbf{H}_{\text{in}}| = 3$, and $P_{\max}/P_{\text{in}} = 1.5$. The local E and H fields are definitely less enhanced than those in the coaxial PlC.

It is also interesting to compare the coaxial PlC with other PlCs including the layer(s) of perforated metallic film(s). Resonant E, H, and P fields were evaluated in stacked complementary (sc) PlCs[18,19] and a typical fishnet metamaterial;[20] the former is a stacked layer structure of a layer of perforated metallic film and a layer of the metallic nanostructure complementary to the shape of perforation. The local E and H fields were at most fivefold enhanced in the sc-PlCs, and the local P fields were also at most fivefold enhanced in the sc-PlCs and the metamaterial. Thus, the local mode at 1100 nm and $\theta = 10^\circ$ in the coaxial PlC was found to be a mode associated with highly enhanced local EM fields in the PlCs including perforated metallic films.

As a resonant mode in a 50-nm metallic gap, the local mode at 1100 nm and $\theta = 10^\circ$ shows highly enhanced fields, which are distributed inside the annular slit. It is worth noting that, in dimers of metallic nanoparticles or nanorods, even 5-nm gaps result in large reduction in the enhancement factor of $|\mathbf{E}_{\max}|/|\mathbf{E}_{\text{in}}|$ in comparing with the 0.5-nm gap, and have the enhancement factor of about 10.[21,22] As the gaps increase up to 50 nm, further tenfold reduction takes place in the dimer structures. In the dimer structure of 0.5-nm gap, an extremely enhanced spot of $|\mathbf{E}_{\max}|/|\mathbf{E}_{\text{in}}| \gtrsim 10^2$ can appear at the center of the dimer, even when nonlocal responses are taken into account;[21,22] at the same time, the hot spot is extremely tiny, typically 1 nm^3. It thus turns out that the PlC of coaxial structure becomes a practical option when 50-nm gaps are preferred in experimental conditions such that a dilute solution is used and expected to be excited rather uniformly.

V. SUMMARY

We clarified the resonant modes in PlCs of coaxial structure from measured optical spectra and numerical calculations. It was found that, in the wavelength range where reduced SPP modes overlap, a local mode appears in the coaxial PlC. The resonant local-EM-field enhancements inside the coaxial metallic nanostructure were comprehensively examined in the E, H, and P fields. It was shown that the local mode dominantly induced in the annular slit of 50-nm width has the largest enhancement factors of 10 and 62 in the E and P fields, respectively, and that the factors are three- to tenfold larger than those in other PlCs of perforated metallic nanostructures.

ACKNOWLEDGMENTS

One of the authors (M.I.) would like to thank Cyberscience Center, Tohoku University for supporting large-scale computations, JSPS KAKENHI (No. 22760047), and JST, PRESTO for their financial support. This study was partially supported by the New Energy and Industrial Technology Development Organization (NEDO).

*iwanaga.masanobu@nims.go.jp

[1] C. Genet and T. W. Ebbesen, Nature (London) **445**, 39 (2007).

[2] F. I. Baida and D. VanLabeke, Phys. Rev. B **67**, 155314 (2003).

[3] F. I. Baida, D. VanLabeke, G. Granet, A. Moreau, and A. Belkhir, Appl. Phys. B **79**, 1 (2004).

[4] W. Fan, S. Zhang, B. Minhas, K. J. Malloy, and S. R. J. Brueck, Phys. Rev. Lett. **94**, 033902 (2005).

[5]F. I. Baida, A. Belkhir, D. VanLabeke, and O. Lamrous, Phys. Rev. B **74**, 205419 (2006).
[6]S. M. Orbons, D. Freeman, B. Luther-Davies, B. C. Gibson, S. T. Huntington, D. N. Jamieson, and A. Roberts, Physica B **394**, 176 (2007).
[7]Y. Poujet, J. Salvi, and F. I. Baida, Opt. Lett. **32**, 2942 (2007).
[8]S. Wu, Q. Wang, X. Yin, J. Li, D. Zhu, S. Liu, and Y. Zhu, Appl. Phys. Lett. **93**, 101113 (2008).
[9]S. P. Burgos, R. de Waele, A. Polman, and H. A. Atwater, Nat. Mater. **9**, 407 (2010).
[10]P. B. Catrysse and S. Fan, Appl. Phys. Lett. **94**, 231111 (2009).
[11]F. Neubrech, A. Pucci, T. W. Cornelius, S. Karim, A. García-Etxarri, and J. Aizpurua, Phys. Rev. Lett. **101**, 157403 (2008).
[12]M. Moskovits, Rev. Mod. Phys. **57**, 783 (1985).
[13]K. Kneipp, Phys. Today **60**, 40 (2007).
[14]L. Li, J. Opt. Soc. Am. A **14**, 2758 (1997).
[15]L. Li, J. Opt. Soc. Am. A **13**, 1024 (1996).
[16]COMSOL Multiphysics [http://www.comsol.com].
[17]A. D. Rakić, A. B. Djurišić, J. M. Elazar, and M. L. Majewski, Appl. Opt. **37**, 5271 (1998).
[18]M. Iwanaga, Opt. Express **18**, 15389 (2010).
[19]M. Iwanaga, Phys. Rev. B **82**, 155402 (2010).
[20]M. Iwanaga, Opt. Lett. **36**, 2504 (2011).
[21]F. J. García de Abajo, J. Phys. Chem. C **112**, 17983 (2008).
[22]J. M. McMahon, S. K. Gray, and G. C. Schatz, Nano Lett. **10**, 3473 (2010).